Automotive Science and Engineering, Vol. 16, No. 2, (2026), 5010-5023

Iran University of Science and Technology

Automotive Science and Engineering

Journal Homepage: ase.iust.ac.ir

ISSN: 2008-9899

# Coordinated Control of Torque Vectoring & Active Rear Camber for Autonomous Vehicle Path-Tracking under Limit Conditions

**Mohammad Dehghan Manshadi, Behrooz Mashhadi***

School of Automotive Engineering, Iran University of Science and Technology

**ARTICLE INFO**

**Article history**:

Received : 29 Dec 2025

Accepted: 26 Mar 2026

Published: 23 Apr 2026

**Keywords**:

Autonomous vehicles

Model Predictive Control (MPC)

Active Rear Camber (ARC)

Torque Vectoring Control (TVC)

Limit handling

Control allocation

**ABSTRACT**

Path-tracking for autonomous vehicles at physical handling limits is severely challenged by nonlinear tire saturation, which degrades conventional Active Front Steering (AFS) systems. This study proposes a hierarchical control architecture coordinating AFS, Torque Vectoring Control (TVC), and Active Rear Camber (ARC) to enhance path-tracking accuracy under limit driving conditions. An upper-level Linear Model Predictive Control (LMPC) algorithm is designed to calculate the virtual corrective yaw moment and the optimal rear camber angle. Simultaneously, a lower-level three-mode Quadratic Programming (QP) framework dynamically allocates torques based on instantaneous tire friction capacities. MATLAB/CarSim co-simulations of severe Double Lane Change (DLC) maneuvers validate the system's efficacy. Quantitatively, during a 140 km/h maneuver on dry asphalt, the proposed fully integrated system expands the maximum achievable lateral acceleration to 0.8g. Compared to the baseline AFS configuration, it significantly reduces the root-mean-square (RMS) and peak lateral tracking errors by 32% (to 0.239 m) and 27% (to 0.687 m), respectively, while concurrently decreasing the peak steering demand by 27%. Furthermore, under low-friction critical conditions (60 km/h, $\mu = 0.5$), the controller effectively limits sideslip oscillations and prevents vehicle spin-out. Ultimately, the formulated hierarchical framework manages the over-actuation dynamically, yielding a peak execution time that consumes only 74% of the real-time step limit, providing a highly viable and computationally efficient strategy for automotive Electronic Control Unit (ECU) implementation.

## 1. Introduction

### 1.1. Path Tracking Challenges

The evolution of autonomous vehicle (AV) technology possesses the potential to revolutionize modern transportation by reducing traffic accidents and optimizing traffic flow efficiency. In this context, electric vehicles (EVs) have emerged as an ideal platform for implementing autonomous driving systems due to their wire-controlled technologies and over-actuated configurations [1]. A fundamental objective within these motion control systems is to precisely guide the vehicle along a predefined path across a wide spectrum of operating conditions [2]. Nevertheless, maintaining a robust compromise between minimizing path-tracking errors and ensuring lateral stability remains a highly complex control

*Corresponding Author

Email Address: b_mashhadi@iust.ac.ir

https://doi.org/10.22068/ase.2026.751

challenge, particularly at elevated speeds and during aggressive maneuvers [3]. Under these limit operating conditions, the highly coupled vehicle and tire dynamics transition into a severely nonlinear regime, causing tire forces to rapidly approach their physical adhesion limits and undergo saturation [4]. To manage these complex dynamics and conflicting objectives, Model Predictive Control (MPC) is widely adopted [5], owing to its capability to regulate multi-variable systems, enforce actuator constraints, and optimize future behavior.

### 1.2. Related Works

To address these challenges and prevent instability under limit conditions, recent research can be categorized into three areas: 1) control algorithms, 2) integrated chassis architectures, and 3) advanced actuator combinations.

In the first area, research mainly focuses on improving MPC to handle dynamic uncertainties. For example, an adaptive MPC strategy has been developed to enforce constraints on the yaw rate boundary while adapting to path curvature [6]. Similarly, tracking adaptability can be enhanced by dynamically adjusting predictive horizons and weight matrices to handle varying vehicle dynamics [7]. Furthermore, a two-layer predictive controller utilizing curvature adaptation has been introduced to strictly manage the active front steering (AFS) angle during high-speed driving [8]. Other method use online optimization [9] to adjust commands. Robust approaches, like tube-based MPC [10], ensure safety against model errors. However, a major physical limit remains: these methods rely only on active front steering (AFS). When tire capacities saturate during high lateral accelerations, better algorithms alone cannot overcome the physical limits of tire forces, leaving the vehicle unstable.

To overcome AFS limits, combining AFS with torque vectoring control (TVC) or direct yaw moment control (DYC) is a common architectural solution [3]. Reviews [11] show that current research heavily favors coordinating these two systems. By independently distributing longitudinal forces, researchers can generate corrective yaw moments. In this framework, a real-time nonlinear MPC combined with explicit path replanning modules is utilized to stabilize sideslip on slippery roads [12]. Concurrently, real-time predictive controllers have been formulated to coordinate AFS and DYC to minimize tracking errors and lateral slip in limit driving conditions [13]. For four-wheel independent drive (4WID) vehicles, fractional-order MPC [14] and multi-layer architectures [15] rely entirely on torque distribution for lateral stability. Other methods explore combined-slip control [16], yaw moment allocation [17], and differential braking [18]. The coordination of AFS and DYC clearly improves tracking in critical dynamic maneuvers through integrated chassis architectures [19]. This synergistic optimization of front steering and direct yaw control is also highly effective for distributed-drive electric vehicles [20]. including autonomous racing [21], with some studies focusing solely on TVC without steering [22]. Still, lateral force in these setups is strictly limited by the tire's slip characteristics.

To achieve ultimate agility, adding a rear-axle actuator to directly manipulate lateral forces is necessary. Within advanced actuator configurations, the standard approach uses four-wheel steering (4WS) and rear-wheel steering (RWS) [23] To achieve the highest level of agility during extreme obstacle avoidance, an over-actuated platform combining 4WS and 4WD has been utilized [24]. Recent studies use these actuators for emergency maneuvers, combining predictive frameworks with 4WS for high-speed overtaking [25]. Comparisons show 4WS provides better stability than classical setups [26]. Similarly, combining TVC and RWS improves handling on low-friction surfaces [27], and reviews of 4WID-4WIS systems confirm the value of linking torque vectoring with independent steering [28]. Although RWS helps by changing the tire sideslip angle, it has a fundamental flaw at the handling limits. When the tire reaches its saturation zone, lateral force generation drops. Consequently, turning the rear wheels further via RWS cannot produce more lateral force, creating a physical bottleneck. If the friction circle is fully used by combined slip, the added steering angle only increases drag without providing the necessary cornering force.

To break this bottleneck, the less-explored active camber (AC) actuator offers unique potential. While RWS relies on the tire's existing, saturated capacity, active camber directly changes how tire forces are generated [29]. By tilting the wheel, it expands the tire's force limits by increasing cornering stiffness and generating camber thrust. Unlike sideslip forces that drop quickly at high angles, camber thrust provides extra lateral force as the tire approaches its non-linear limit. Studies show that active camber improves lateral capability even when traditional steering saturates. For example, coordinating active camber on all four wheels greatly increases lateral force capacity, freeing lateral stability from longitudinal slip limits [30]. Crucially, a more optimal approach—using



[ DOI: 10.22068/ase.2026.751 ]

active camber exclusively at the rear axle for stability—remains unexplored. Despite its physical potential, most integrated chassis research still relies on classical actuators [31], and the specific role of active rear camber in limit conditions is not fully understood. While MPC is a powerful tool to allocate forces and enforce physical limits, true performance gains in extreme scenarios depend on choosing actuators that can actually shift the tire's physical boundaries [5].

### 1.3. Research Contribution

Accordingly, to exploit the physical capabilities of the vehicle chassis under limit handling conditions, this study presents a coordinated hierarchical control strategy for the simultaneous management of active front steering (AFS), torque vectoring control (TVC), and active rear camber (ARC). The primary objective is to evaluate the physical synergy of these active actuators during aggressive maneuvers, specifically analyzing how an exclusive active rear camber mechanism can generate independent camber thrust to relieve the lateral workload of saturated front tires.

The major contributions of this work are focused on practical implementation and computational feasibility. First, an upper-level linear model predictive controller (LMPC) is formulated to calculate optimal virtual corrective inputs, incorporating a hard constraint on the vehicle sideslip angle to guarantee lateral stability while maintaining real-time computational efficiency. Second, a lower-level control allocation layer based on a three-mode Quadratic Programming (QP) algorithm is developed, utilizing a continuous weight scheduling strategy based on a phase-plane stability index to smoothly transition between operational modes without control chattering. Finally, the proposed framework is validated in a MATLAB/CarSim environment under severe high-speed dry and low-friction slippery maneuvers, quantitatively assessing the trade-off between tracking accuracy and normalized control effort, and demonstrating real-time execution feasibility within standard ECU step limits.

The remainder of this paper is organized as follows: Section 2 establishes the vehicle and tire dynamic models incorporating the camber effect. Section 3 delineates the design of the model predictive control strategy and actuator coordination layer. Section 4 illustrates and discusses the co-simulation results under limit conditions. Finally, Section 5 presents the concluding remarks.

## 2. Vehicle and Tire System Modeling

In this section, the baseline mathematical models describing the vehicle dynamics and tire subsystems are presented. The primary objective of this modeling framework is to establish a representation that is both accurate and computationally efficient, thereby enabling real-time implementation of the predictive controller with minimal hardware overhead. Accordingly, the narrative of this section initiates with the global chassis dynamics, proceeds to the modulation of tire physical forces incorporating the rear active camber effect, and concludes with the state-space formulation of the system.

### 2.1. Vehicle Dynamics Model

To describe the planar motion of the vehicle—specifically the lateral and yaw dynamics—a two-degree-of-freedom (2-DOF) single-track (bicycle) model is utilized. The physical schematic and the free-body diagram of the forces acting on this model are illustrated in Figure 1.

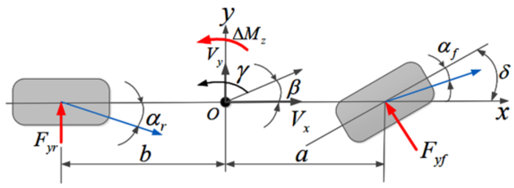


**Figure 1:** 2-DOF Vehicle dynamics model

Assuming a small front steering angle ($\delta_f$) and neglecting high-order suspension dynamics (such as roll and pitch), the differential equations governing the lateral motion and the yaw rate ($r$) are expressed as follows [6]:

$$F_{yf} + F_{yr} = m(\dot{v} + ru) \tag{1}$$

$$aF_{yf} - bF_{yr} = I_z\dot{r} \tag{2}$$

where $m$ represents the total vehicle mass, $I_z$ denotes the yaw moment of inertia about the vertical axis at the center of gravity (CG), $u$ and $v$ are the longitudinal and lateral velocities of the vehicle in the body-fixed coordinate system, respectively, and $r$ is the yaw rate. Additionally, $a$ and $b$ signify the distances from the CG to the front and rear axles, respectively. Finally, $F_{yf}$ and $F_{yr}$ denote the total lateral forces aggregated at the front and rear tires, encapsulating the combined effects of steering and camber:

$$F_{yf} = F_{yf_\alpha} \tag{3}$$

$$F_{yr} = F_{yr_\alpha} + F_{yr_\gamma} \tag{4}$$



[ DOI: 10.22068/ase.2026.751 ]

where $F_{yi,\alpha}$ and $F_{yi,\gamma}$ represent the lateral force components induced by the tire slip angle and the camber angle, respectively.

The adoption of the small steering angle approximation is practically justified even during high-speed evasive maneuvers, as large steering inputs would instantly exceed the tire's cornering capacity and induce unrecoverable instability. Furthermore, neglecting roll dynamics and lateral load transfer in this upper-level predictive model is an intentional design choice to ensure strict computational efficiency for real-time LMPC execution. The inherent unmodeled dynamics and physical nonlinearities caused by vertical load transfer are systematically compensated for within the lower-level Control Allocation (QP) layer by dynamically adapting to the instantaneous vertical tire loads within the explicit friction circle constraints, the allocation layer acts as a robust compensatory mechanism against the simplified assumptions of the upper-level model.

### 2.2. Tire Dynamics and Camber Influence

Following the derivation of the vehicle body equations of motion, formulating the tire-road interaction forces becomes essential as they constitute the primary determinant of vehicle dynamic behavior. In this study, a linear tire model is utilized to develop the state-space formulation for the upper-level controller, while an adaptive nonlinear model is employed within the control allocation layer.

#### 2.2.1. Linear Tire Model

During conventional maneuvers characterized by lateral accelerations below $0.4g$, the tire behavior exhibits high correlation with linear models [29]. Assuming small tire slip angles (typically less than 6°), the linear lateral tire force equations are derived as:

$$F_{yf_\alpha} = -C_{\alpha_f}\alpha_f \tag{5}$$

$$F_{yr_\alpha} = -C_{\alpha_r}\alpha_r \tag{6}$$

where $C_{\alpha_i}$ denotes the cornering stiffness of the front and rear tires, defined as positive constant values. Based on the vehicle kinematics, the front $(\alpha_f)$ and rear $(\alpha_r)$ tire slip angles are defined as:

$$\alpha_f = \beta + \frac{ar}{u} - \delta_f \tag{7}$$

$$\alpha_r = \beta - \frac{br}{u} \tag{8}$$

where β represents the vehicle sideslip angle, is the yaw rate, and $\delta_f$ signifies the front wheel steering angle.

#### 2.2.2. Adaptive Tire Model for TVC

A key requirement in torque vectoring control systems is the physical management of tire saturation within the friction circle boundary ($F_x^2 + F_y^2 \le \mu^2 F_z^2$). With a known vertical load ($F_z$) and road friction coefficient (μ), the maximum allowable longitudinal force is determined based on the physical limits of the tire [18]. To alleviate the computational burden associated with solving the complex nonlinear Pacejka Magic Formula online, an alternative nonlinear mathematical model has been developed based on CarSim data, which adopts the concept of adapting the tire cornering stiffness online using the secant slope from the origin [32]. The formulation of this nonlinear model is structured as a combination of two single-variable functions:

$$C_\alpha = k(\alpha) C_s F_z \tag{9}$$

where $C_s$ represents the zero-slip slope of the lateral tire force curve for static tire vertical loads. Additionally, $f(\alpha)$ denotes a dimensionless slope correction factor based on the tire operating point on the normalized $(F_y/F_z)$ curve, which models the nonlinear tire behavior at slip angles exceeding 6°.

To accurately capture the dynamic limits of each wheel during severe maneuvers, the instantaneous vertical load ($F_{z,ij}$) is continuously updated by accounting for both longitudinal and lateral load transfers:

$$F_{z,ij} = F_{z,ij_s}\left(1 + \left(-\frac{2a_y h_{cg}}{gT_w}\right)^{j+1}\right) + \left(-\frac{m a_x h_{cg}}{2l}\right)^{i} \tag{10}$$

where the subscripts $ij$ denote the front-left, front-right, rear-left, and rear-right wheels, respectively. $F_{z,ij_s}$ represent the static vertical tire loads on the front and rear axles. Furthermore, $a_x$ and $a_y$ denote the longitudinal and lateral accelerations, $h_{cg}$ is the center of gravity height, $T_w$ is the track width, $l$ is the vehicle wheelbase, $m$ is the total vehicle mass, and $g$ is the gravitational acceleration.

Based on instantaneous kinematic relations, the tire slip angle $(\alpha_i)$ is subsequently calculated for each wheel individually. Using these updated vertical loads and slip angles, the generated lateral tire force is computed via Equation (9). Finally, this lateral force is evaluated against the physical friction circle boundary to determine the exact remaining capacity of each individual tire to produce longitudinal forces.

This adaptive model has been validated against the nonlinear Pacejka model (see Figure 2), yielding a maximum relative error of merely 4% under limit lateral accelerations (approximately $1g$), thereby demonstrating high fidelity with



[ DOI: 10.22068/ase.2026.751 ]

minimal computational overhead. Specifically, the execution time averages 0.6 milliseconds, with a peak of 3 milliseconds per control step (consuming only 13% of the controller step time) within the MATLAB environment, robustly substantiating its viability for real-time ECU implementation.

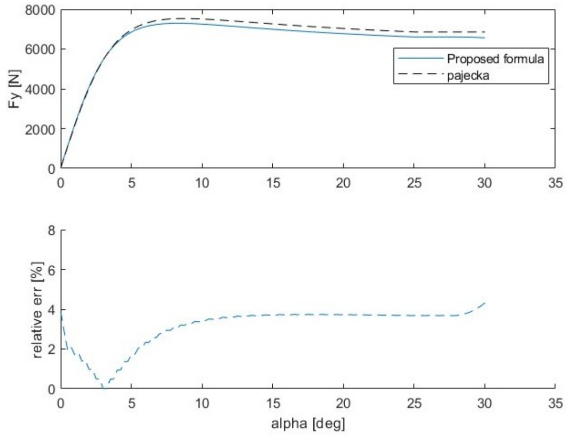


**Figure 2:** Comparison of lateral tire force between the proposed model and the Pacejka tire model

Furthermore, the validation of the adaptive tire model under an aggressive maneuver with a lateral acceleration of $0.7g$ against CarSim software data demonstrates high fidelity with minimal computational overhead (see Figure 3).

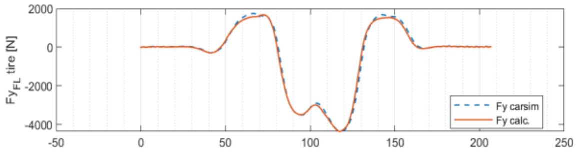


**Figure 3:** Lateral tire force validation of the proposed model compared to CarSim

### 2.2.3. Rear Active Camber Model

The lateral force generated by the ARC mechanism offers a unique physical potential to produce lateral forces without necessitating an increase in the tire slip angle [30]. Under the assumption of a constant longitudinal velocity, the effect of lateral load transfer is neglected, and the suspension behavior is assumed to be linear. This justifies considering the camber stiffness coefficient as a constant value evaluated under the static load conditions of the rear wheels:

$$F_{yr_\gamma} = C_\gamma \gamma_r \tag{11}$$

where $F_{y\gamma}$ is the independent lateral force component resulting from the camber at the rear wheels, $C_\gamma$ denotes the tire camber thrust stiffness, and $\gamma_r$ represents the active camber angle applied to the rear axle. The positive direction of the camber angle for both the left and right wheels is defined as a rotation about the vehicle's longitudinal axis in the direction of a positive roll angle.

### 2.3. State-Space Formulation

By combining the force components derived from the tire sideslip angle and the active rear camber (Equations (3–8) and (1١)), the total lateral forces acting on the front and rear axles are extracted as follows:

$$F_{yf} = -C_{\alpha_f}\left(\beta + \frac{ar}{u} - \delta_f\right) \tag{12}$$

$$F_{yr} = -C_{\alpha_r}\left(\beta - \frac{br}{u}\right) + C_\gamma \gamma_r \tag{13}$$

Substituting these expressions into the vehicle body equations of motion (Equations (1–2)), applying the small front steering angle assumption ($\delta_f < 6°$), and simplifying the terms yields the lateral dynamics equations. These equations serve as the foundation for the model predictive controller development:

$$\dot{\beta} = -\frac{C_{\alpha_f}+C_{\alpha_r}}{mu}\beta - \left(\frac{aC_{\alpha_f}-bC_{\alpha_r}}{mu^2}+1\right)r + \frac{C_{\alpha_f}}{mu}\delta_f + \frac{C_\gamma}{mu}\gamma_r \tag{14}$$

$$\dot{r} = -\frac{\left(aC_{\alpha_f}-bC_{\alpha_r}\right)}{I_z}\beta - \frac{\left(a^2C_{\alpha_f}+b^2C_{\alpha_r}\right)}{I_z u}r + \frac{aC_{\alpha_f}}{I_z}\delta_f - \frac{bC_\gamma}{I_z}\gamma_r + \frac{\Delta M_z}{I_z} \tag{15}$$

Consequently, the continuous-time state-space representation of the system is formulated as:

$$\dot{X} = AX + BU \tag{16}$$

where the system state vector is defined as $X = [Y \quad \psi \quad \beta \quad r]^T$ and $U = \left[\delta_f \quad \gamma \quad \Delta M_z\right]^T$ and The system matrix ($A$) and input matrices ($B$) are structurally formulated as follows:

$$A = \begin{bmatrix} 0 & u & u & 0 \\ 0 & 0 & 0 & 1 \\ 0 & 0 & -\frac{C_{\alpha_f}+C_{\alpha_r}}{mu} & -\frac{aC_{\alpha_f}-bC_{\alpha_r}}{mu^2}-1 \\ 0 & 0 & -\frac{aC_{\alpha_f}-bC_{\alpha_r}}{I_z} & -\frac{a^2C_{\alpha_f}+b^2C_{\alpha_r}}{I_z u} \end{bmatrix}$$

$$B = \begin{bmatrix} 0 & 0 & 0 \\ 0 & 0 & 0 \\ \frac{C_{\alpha_f}}{mu} & \frac{C_\gamma}{mu} & 0 \\ \frac{aC_{\alpha_f}}{I_z} & -\frac{bC_\gamma}{I_z} & \frac{1}{I_z} \end{bmatrix} \tag{17}$$

Within this formulation, the direct influence of the active rear camber stiffness ($C_\gamma$) is explicitly

embedded within the input matrix $B$. This demonstrates how the active camber actuator provides an additional, direct degree of freedom for lateral control, operating effectively alongside the front steering commands.

### 2.4. Actuator Constraints and Hardware Parameters

To ensure high-fidelity simulation and systematically enforce physical boundaries on the actuators within the control allocation layer, the hardware specifications of the vehicle subsystems are incorporated based on realistic parameters:

- Powertrain Configuration (In-Wheel Motors): The TVC system is implemented via four independent in-wheel electric motors. The performance characteristics and constraints of these actuators are calibrated based on the commercial data of the Protean Electric Pd18 in-wheel motor.
- Tire Structural Parameters: The linear and boundary parameters of the tire, including cornering stiffness ($C_{\alpha_f}, C_{\alpha_r}$), camber thrust stiffness ($C_\gamma$), and longitudinal stiffness, are extracted from the nonlinear tire behaviors within the CarSim environment to maximize the correlation between the control model and the actual vehicle platform.
- Steering System Architecture: The steering mechanism is modeled in CarSim based on Ackerman geometry, which inherently introduces a discrepancy between the steering angles of the inner and outer wheels. By averaging this geometric relationship, the overall gear ratio between the steering wheel and the road wheels is established.

## 3. Control and Allocation Strategy

To optimally exploit the physical capabilities of the chassis actuators under limit conditions, a hierarchical control strategy is adopted. This architecture comprises an upper-level Model Predictive Controller (MPC) designed to calculate the virtual corrective yaw moment and the active camber angle, alongside a lower-level control allocation (CA) framework formulated via Quadratic Programming (QP) to optimally distribute the torque among the independent in-wheel motors (see Figure 4).

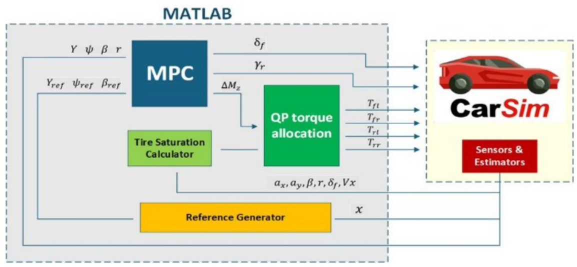


**Figure 4:** The co-simulation framework

### 3.1. Upper-Level Path Tracking Controller

This section details the formulation of the upper-level Linear Model Predictive Controller (LMPC), which is responsible for calculating the optimal virtual corrective inputs to follow the reference trajectory while maintaining vehicle stability.

#### 3.1.1. Discretization and Augmented Model

A fundamental prerequisite for implementing the predictive algorithm is the discretization of the continuous-time system model with a sampling time $T_s$. The discretized matrices are obtained as $A_d = e^{AT_s}$, $B_d = B\int_0^{T_s} e^{A\tau}\,d\tau$ and $C_d = C$. To ensure zero steady-state tracking error and penalize the rate of change of the control inputs $\Delta u(k) = u(k) - u(k-1)$, the discrete model is transformed into an augmented state-space representation. Defining the augmented state vector $\xi(k) = [x(k)\ ,\ u(k-1)]^T$, the modified system is formulated as:

$$\xi(k+1) = \bar{A}_d \xi(k) + \bar{B}_d \Delta u(k) \tag{18}$$

$$y(k) = \bar{C}_d \xi(k) \tag{19}$$

where the augmented system matrices are structurally defined as:

$$\bar{A}_d = \begin{bmatrix} A_d & B_d \\ 0 & I \end{bmatrix},\quad \bar{B}_d = \begin{bmatrix} B_d \\ I \end{bmatrix},$$

$$\bar{C}_d = [C_d \quad 0] \tag{20}$$

By iterating the augmented model over the prediction horizon ($N_p$) and control horizon ($N_c$), the future output sequence can be compactly expressed in matrix form as:

$$Y(k+1) = S_x \xi(k) + S_u \Delta U(k) \tag{21}$$

where $S_x$ and $S_u$ are the standard predictive tracking matrices.

#### 3.1.2. MPC Optimization and Cost Function

To simultaneously minimize the path-tracking error and penalize excessive control energy, the standard objective function for the MPC optimization is defined as:



[ DOI: 10.22068/ase.2026.751 ]

$$J = \sum_{i=1}^{N_p} \left(\Gamma_{xi}\left(y(k + i) - y_{ref}\right)\right)^2 + \sum_{i=0}^{N_c} \left(\Gamma_{ui}\left(\Delta u(k + i)\right)\right)^2 \quad (22)$$

For real-time computational efficiency, this objective is converted into a standard Quadratic Programming (QP) form. By defining the tracking error as $E(k) = S_x\xi(k) - Y_{ref}$, the cost function is simplified to:

$$J = \Delta U(k)^{\mathrm{T}} H \Delta U(k) + \Delta U(k)^{\mathrm{T}} f + E(k)^{\mathrm{T}} \Gamma_x E(k) \quad (23)$$

where the Hessian matrix and gradient vector are derived as $H = \Gamma_u + S_u^T \Gamma_x S_u$ and $f = 2S_u^T \Gamma_x E(k)$ (ignoring the constant term for optimization).

### 3.1.3. Operational Constraints

To adapt the controller to the actual hardware limitations and prevent actuator saturation, hard constraints are systematically imposed on both the physical amplitude and the slew rate of the control inputs:

$$U_{min} \leq u(k) \leq U_{max} \quad (24)$$

$$\Delta U_{min} \leq \Delta u(k) \leq \Delta U_{max} \quad (25)$$

Crucially, while the upper-level predictive controller operates based on a simplified linear 2-DOF bicycle model, it proactively guarantees vehicle lateral stability by explicitly constraining the vehicle dynamics. To ensure that the tire forces remain within their stable, linear regions and to rigorously prevent unrecoverable spin-out under limit handling, a hard constraint is enforced on the vehicle sideslip angle ($\beta$) [32]:

$$-tan^{-1}(0.025 \times \mu g/V_x^2) \leq \beta \leq tan^{-1}(0.025 \times \mu g/V_x^2) \quad (26)$$

By directly incorporating Equation (26) into the cost function, the LMPC fundamentally restricts the lateral dynamics from exceeding the physical handling boundaries. This crucial constraint bridges the theoretical gap between the linear prediction model and the highly nonlinear reality of the vehicle, ensuring that the simplified 2-DOF formulation remains highly valid and robust even during aggressive evasive maneuvers.

## 3.2. Lower-Level Control Allocation Framework (QP)

The objective of the lower-level allocation layer is to accurately distribute the virtual commands calculated by the MPC among the four independent electric motors, defined by the control vector $U = \left[F_{xfl}, F_{xfr}, F_{xrl}, F_{xrr}\right]^T$. This is formulated as a QP problem, $J_j = \frac{1}{2}U^T H_j U + f_j^T U$, explicitly accounting for the dynamic boundaries of the tire friction circle [3].

### 3.2.1. Optimization Formulation and Multi-Mode Switching

In integrated chassis systems, multi-objective optimization and mode selection frameworks are widely deployed to balance conflicting dynamic criteria, such as ride comfort versus handling stability [33]. Inspired by this structural philosophy, our allocation layer dynamically shifts its priority from precise longitudinal tracking to absolute lateral stability as the dynamic severity increases. To systematically govern these transitions, a dynamic switching logic is formulated based on a Phase-Plane Stability Index and individual tire saturation flags. Phase-plane boundaries are highly effective tools in defining vehicle stability envelopes [34]. Accordingly, the physical Stability Index ($SI$) is defined by normalizing the instantaneous yaw rate ($r$) and sideslip angle ($\beta$) against their physical boundaries:

$$SI = \sqrt{\left(\frac{r}{r_{\max}}\right)^2 + \left(\frac{\beta}{\beta_{\max}}\right)^2} \quad (27)$$

where the physical limits on a given road surface are defined as $r_{\max} = \frac{\mu g}{V_x}$ and $\beta_{\max} = \arctan(0.02\mu g)$.

To inherently avoid undesirable chattering between control modes during rapid transient maneuvers, instead of relying on discrete hysteresis bands, a continuous weight scheduling strategy is adopted. The tracking weight ($W_{Mz}$) inside the optimization cost function is dynamically updated as a continuous function of $SI$. This guarantees smooth control allocations without sudden torque jumps. Based on this physical index and tire saturation constraints, the three operational modes are strictly thresholded as follows:

- **Mode I (Normal Driving):** Triggered when the vehicle is strictly stable ($SI < 0.1$) and no tire has reached its physical friction limit ($\sum \text{saturation\_flags} = 0$). Tires operate in the linear region. Both total longitudinal force ($F_{xd}$) and corrective yaw moment ($M_z$) are enforced as equality constraints ($A_{eq}U = b_{eq}$). The cost function solely minimizes tire workload with $W_{Fd} = 1$ and a dynamically scaled yaw penalty $W_{Mz} = 0.01 \cdot SI$.
- **Mode II (Approaching Saturation):** Triggered during moderate dynamic severity ($0.1 \leq SI < 0.3$) while tires remain unsaturated. Maintaining the yaw moment remains a hard equality constraint, but





[ DOI: 10.22068/ase.2026.751 ]

longitudinal force tracking is relaxed to a soft constraint. The Hessian is modified to penalize longitudinal tracking deviation alongside the dynamically scheduled weight $W_{Mz} = 1 \cdot SI$.

- **Mode III (Limit Handling):** Activated under critical conditions where $SI \geq 0.3$ or when any individual tire physically saturates ($\sum$ saturation_flags $> 0$). Under extremely critical conditions, preventing solver failure and maintaining stability is prioritized; no equality constraints are enforced ($A_{eq} = \emptyset$). Both longitudinal force and yaw moment are treated as soft constraints, with heavily prioritized stability weights scaling quadratically ($W_{Mz} = 1 + 100 \cdot SI^2$) to strictly guarantee physical feasibility and vehicle safety.

### 3.2.2. Actuator and Friction Constraints

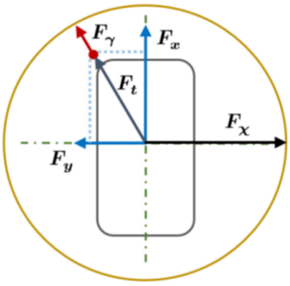


**Figure 5:** Simplified friction circle of tire [22]

For all operational modes, the longitudinal force limits for each tire are instantaneously bounded by the intersection of the tire's physical friction circle (See Figure 5) and the maximum torque capacity ($\tau_{max}$) of the in-wheel motors. The optimization bounds ($lb_d \leq U \leq ub_d$) are explicitly defined as:

$$|F_{xi}| \leq \min\left(\sqrt{(\mu F_{zi})^2 - F_{yi}^2}\ ,\ \frac{\tau_{max}}{r_w}\right) \quad (28)$$

Ultimately, upon solving the QP algorithm and extracting the optimal longitudinal tire forces ($F_{xi}$), the torque command applied to each independent electric motor ($T_i$) is calculated using the effective tire radius ($r_w$):

$$T_i = F_{xi} \times r_w \quad (29)$$

## 4. Simulation and Results

To validate the effectiveness of the proposed hierarchical control architecture, comprehensive co-simulations are conducted. This section details the simulation environment and evaluates the specific contributions of the active chassis actuators under limit handling conditions by comparing the fully integrated system against baseline chassis control configurations.

### 4.1. Simulation Setup

To rigorously evaluate the performance of the proposed hierarchical control architecture, a high-fidelity co-simulation environment is established using MATLAB and CarSim. The vehicle plant is modeled in CarSim using a D-class sedan configuration, which intrinsically incorporates nonlinear suspension kinematics, load transfer effects, and high-order tire dynamics. The predictive controller and the control allocation algorithms are executed within the MATLAB environment. To ensure a comprehensive assessment, the proposed integrated system (AFS+AC+TVC) is benchmarked against three conventional chassis control configurations:

1. AFS: Baseline active front steering operating independently.
2. AFS+TVC: Conventional integrated control without active camber intervention.
3. AFS+AC: Active front steering combined with rear active camber, without torque vectoring.
4. AFS+AC+TVC: The proposed fully integrated control architecture, coordinating all actuators to maximize limit-handling performance.

The standard ISO 3888-1:2018 Double Lane Change (DLC) maneuver has been selected for this study. Subjecting the vehicle to this standardized trajectory provides a rigorous platform for evaluating the performance of advanced stability control systems. The mathematical formulation governing the geometric profile of the reference path is defined by the following equations [20]:

$$Y_{ref}(X) = tan^{-1}\left(d_{y_1}\left(\frac{1}{cosh(z_1)}\right)^2\left(\frac{1.2}{d_{x_1}}\right) - d_{y_2}\left(\frac{1}{cosh(z_2)}\right)^2\left(\frac{1.2}{d_{x_2}}\right)\right) \quad (30)$$

where the parameters $d_{x_1}$, $d_{x_2}$, $d_{y_1}$ and $d_{y_2}$ are constant values set to 21, 20.5, 3.57, and 3.57, respectively. Furthermore, the intermediate variables ($z_i$) are defined as functions of the vehicle's longitudinal displacement ($X$):

$$z_1 = \frac{2.4}{d_{x1}}(X - 70) - 1.2 \quad , \quad z_2 = \frac{2.4}{d_{x2}}(X - 121.5) - 1.2 \quad (31)$$

The key parameters of the vehicle and the controller are summarized in Table 1:





[ DOI: 10.22068/ase.2026.751 ]

**Table 1:** Vehicle and actuator parameters

| Vehicle Parameter | Description | Value | unit |
|---|---|---|---|
| $m_{SM}$ | Vehicle sprung mass | 1370 | kg |
| $m_{UM}$ | Vehicle unsprung mass | 2 x 80 | kg |
| $a$ | Distance from CG to front axle | 1.11 | m |
| $b$ | Distance from CG to rear axle | 1.67 | m |
| $Tw$ | Track width | 1.55 | m |
| $h_{CG}$ | CG height | 0.520 | m |
| $r_w$ | Wheel radius | 0.325 | m |
| $I_z$ | Yaw moment of inertia | 2315 | kg.m$^2$ |
| $C_f$ | Front axle static cornering stiffness | 103920 | N/rad |
| $C_r$ | Rear axle static cornering stiffness | 73637 | N/rad |
| $C_\gamma$ | Rear axle camber stiffness | 6188 | N/rad |
| $T_{m\,max}$ | Maximum continues torque of IWM | 650 | N.m |
| $\omega_b$ | Base speed of IWM | 800 | rpm |
| $n_{G\,steer}$ | Total gear ratio of steering wheel to wheels | 15.84 | - |

To ensure a highly realistic evaluation and address practical implementation challenges, the dynamic behavior of the active rear camber and torque vectoring actuators includes their physical delay characteristics, modeled as first-order lag systems. Additionally, to evaluate the cost-benefit trade-off of the coordinated actuator configurations, a dimensionless control effort index is introduced in this setup. This index normalizes the heterogeneous control inputs (steering angles, camber angles, and in-wheel motor torques) by their physical limits. Mathematically, this dimensionless control effort index ($CE$) is defined by integrating the normalized squared inputs of the Active Front Steering ($\delta_f$), Active Rear Camber ($\gamma_r$), and Torque Vectoring ($T_i$) actuators over the maneuver duration ($t_f$):

$$CE = \int_0^t \left[\left(\frac{\delta_f}{\delta_{\max}}\right)^2 + \left(\frac{\gamma_r}{\gamma_{\max}}\right)^2 + \frac{1}{4}\Sigma_1^4\left(\frac{T_i}{T_{\max}}\right)^2\right]dt \quad (32)$$

where $\delta_{\max}$, $\gamma_{\max}$, and $T_{\max}$ represent the absolute physical saturation limits of the steering angle, rear camber angle, and in-wheel motor torque, respectively. Normalizing these heterogeneous control signals by their respective physical limits ensures that the calculated index accurately reflects the true percentage of actuator utilization, thereby providing a physically consistent metric for the subsequent cost-benefit evaluation.

## 4.2. Limit Handling Analysis: Actuators Effectiveness

To systematically evaluate the contribution of each active chassis subsystem and validate the core hypothesis of this study, the vehicle's dynamic response is analyzed under physical limit conditions where the tires approach their saturation boundaries.

### 4.2.1. High-Speed Maneuver on Dry Asphalt ($\mu = 0.85$)

In the first scenario, the vehicle executes the DLC maneuver at an aggressive speed of 140 km/h on a dry road surface ($\mu = 0.85$). As illustrated in Figure 6 and quantitatively supported by Table 2 and Table 3, the baseline AFS system experiences significant lateral deviation due to the saturation of the front tires cornering capacity. Once the front tires enter the nonlinear friction region, further steering interventions fail to generate the requisite lateral force, resulting in a pronounced path-tracking error.

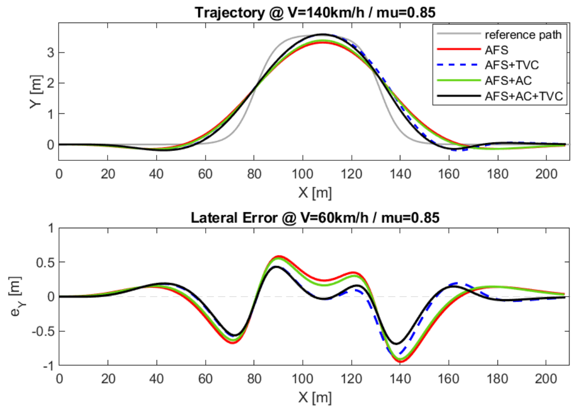


**Figure 6:** Vehicle trajectory tracking performance & Lateral tracking error comparison

**Table 2:** quantitative performance comparison for the **140 $km/h$** DLC maneuver on dry asphalt

| KPI | unit | AFS | AFS +AC | AFS +TVC | AFS +TVC +AC | Improve-ment |
|---|---|---|---|---|---|---|
| $e_{Y_{RMS}}$ | m | 0.352 | 0.328 | 0.275 | 0.239 | +32% |
| $e_{Y_{Max}}$ | m | 0.946 | 0.907 | 0.853 | 0.687 | +27% |
| $e_{\psi_{RMS}}$ | rad | 0.038 | 0.038 | 0.055 | 0.053 | -39% |
| $e_{\psi_{Max}}$ | rad | 0.110 | 0.107 | 0.152 | 0.147 | -34% |
| $a_{y_{Max}}$ | g | 0.679 | 0.718 | 0.758 | 0.800 | +18% |
| $\beta_{Max}$ | deg | 2.78 | 3.00 | 7.81 | 7.18 | -158% |
| $\delta_{f_{Max}}$ | deg | 1.85 | 1.74 | 1.32 | 1.34 | +27% |
| $CE \times 10^{10}$ | - | 4.1 | 137.6 | 56.1 | 652.9 | - |

A detailed comparative analysis of Table 2 reveals the specific contributions of each actuator. Integrating the active camber (AFS+AC) reduces the RMS lateral error by approximately 7% without amplifying the yaw or sideslip tracking errors,




[ DOI: 10.22068/ase.2026.751 ]

demonstrating its capability to safely assist the vehicle without compromising stability. On the other hand, the torque vectoring integration (AFS+TVC) achieves a more substantial 22% reduction in path error; however, this aggressive longitudinal slip intervention slightly degrades the lateral stability margin (increasing peak $\beta$), though it does not lead to spin-out. The superiority of the fully integrated architecture (AFS+RAC+TVC) is distinctly evident. By synergistically combining independent camber thrust and optimal torque vectoring, the RMS lateral tracking error is minimized by 32% (dropping to 0.239 m), and the maximum achievable lateral acceleration is expanded to 0.8g. Furthermore, the maximum front steering angle ($\delta_f$) is notably reduced by 27%. While this aggressive path-tracking performance comes at the cost of an increased peak sideslip angle (1.6 times higher than the baseline), the proposed controller successfully regulates this nonlinear sideslip, securely navigating the 140 km/h maneuver without spin-out. This explicitly confirms that the system prioritizes critical path-following accuracy the primary objective of this study while maintaining the vehicle securely within manageable stability boundaries.

#### 4.2.2. Cost-Benefit and Real-Time Feasibility Analysis

The remarkable 32% improvement in trajectory tracking accuracy naturally necessitates a higher control effort, as indicated by the Control Effort ($CE$) index in Table 2. To justify this energetic cost and verify the practical viability of the controller on standard automotive Electronic Control Units (ECUs), the computational burden of the control allocation layer was analyzed (Table 3).

**Table 3:** Computational burden analysis

| KPI | AFS | AFS +AC | AFS +TVC | AFS +TVC +AC |
|---|---|---|---|---|
| Average Execution Time per Step | 0.0043 | 0.0039 | 0.0064 | 0.0057 |
| Average Percentage of Step Time | 15% | 14% | 23% | 21% |
| Peak Execution Time | 0.0168 | 0.0153 | 0.0289 | 0.0204 |
| Max Percentage of Step Time | 61% | 56% | 105% | 74% |

As presented in Table 3, the baseline AFS utilizes an average of 15% of the controller step time. While the AFS+TVC configuration exhibits a peak execution time that exceeds the step time limit (105%), leading to potential solver overruns, the proposed fully integrated system (AFS+TVC+AC) mitigates this issue. By distributing the workload across three actuators, the proposed system reduces the peak execution time to 74% of the step time, with an average utilization of only 21%. Therefore, the negligible 6% increase in average computational burden compared to the baseline is a highly optimal cost for the substantial 32% benefit in path-tracking accuracy, fully validating the real-time feasibility of the proposed hierarchical framework.

#### 4.2.3. Low-Friction Critical Maneuver ($\mu = 0.5$)

To further isolate the stabilizing effect of the integrated actuators, a critical DLC maneuver is simulated at 60 km/h on a slippery road surface ($\mu = 0.5$). On such low-friction surfaces, the tire saturation boundary shrinks significantly, making the vehicle highly susceptible to spin-out and loss of control.

Figure 7 presents the comprehensive dynamic states of the vehicle during this maneuver. The baseline AFS controller exhibits severe performance degradation, with the sideslip angle ($\beta$) oscillating violently and exceeding physical stability limits, which is a clear indicator of incipient lateral instability. Conversely, the fully integrated architecture strictly suppresses these instabilities through three key mechanisms:

1. Enhanced Sideslip Stability: As shown in Figure 7(d), the sideslip angle is strictly damped and confined within a narrow, safe envelope around zero, fundamentally preventing the vehicle from drifting into an unrecoverable state on the slippery surface.
2. Path Error Minimization: The lateral tracking error is significantly reduced compared to the baseline, ensuring the vehicle remains strictly within the intended lane boundaries despite the low friction.
3. Actuator Workload Relief: Analyzing the front steering command reveals that the peak steering angle demanded by the integrated system is reduced by approximately 1° compared to the standalone AFS. By avoiding excessive steering angles which would merely induce additional drag and deepen tire saturation the controller intelligently distributes the stabilizing effort to the active camber and TVC systems.

Ultimately, the fully integrated architecture definitively confirms that the optimal coordination of active camber and torque vectoring not only maximizes trajectory tracking accuracy but strictly guarantees dynamic stability under severe friction constraints.



[ DOI: 10.22068/ase.2026.751 ]

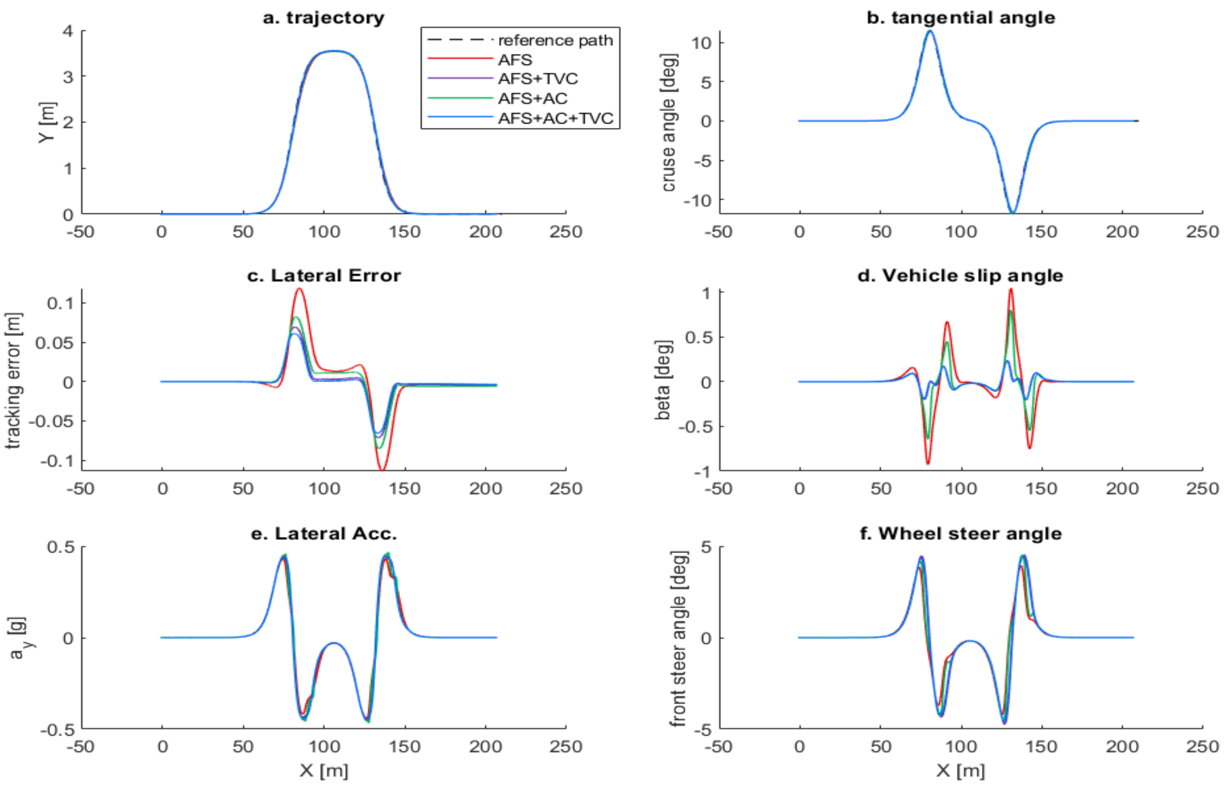


**Figure 7:** Comprehensive 6-panel dynamic states of the vehicle running 60 km/h under low-friction conditions

## 4.3. Control Allocation and Internal Dynamics

To gain deeper physical insight into the hierarchical control framework, the internal behavior of the active subsystems and the lower-level Quadratic Programming (QP) allocation layer is analyzed during a high-speed maneuver (120 km/h on dry asphalt).

As quantitatively supported by Table 2 and the dynamic responses in Figure 7 and Figure 8, the peak front steering angle ($\delta_f$) consistently remains below 6° across all simulated extreme maneuvers. This observation physically validates the small-angle approximation utilized in the upper-level linear 2-DOF vehicle model. Consequently, the dominant source of vehicle nonlinearity is isolated to the tire cornering stiffness degradation and friction saturation, rather than the steering geometry. This robustly justifies the proposed hierarchical architecture: the upper-level MPC operates efficiently in the linear domain, while the severe tire nonlinearities are explicitly and securely managed by the lower-level control allocation layer.

The detailed internal dynamics of this allocation process are depicted in Figure 8. The last panel illustrates the dynamic transition of the TVC optimization modes. The QP algorithm intelligently switches between the predefined operational modes (Modes I, II, and III) in real-time, rapidly adapting to the instantaneous tire saturation limits. This multi-mode switching ensures that the allocation layer prioritizes vehicle stability (yaw moment tracking) over pure longitudinal tracking when the friction circle boundaries are approached.

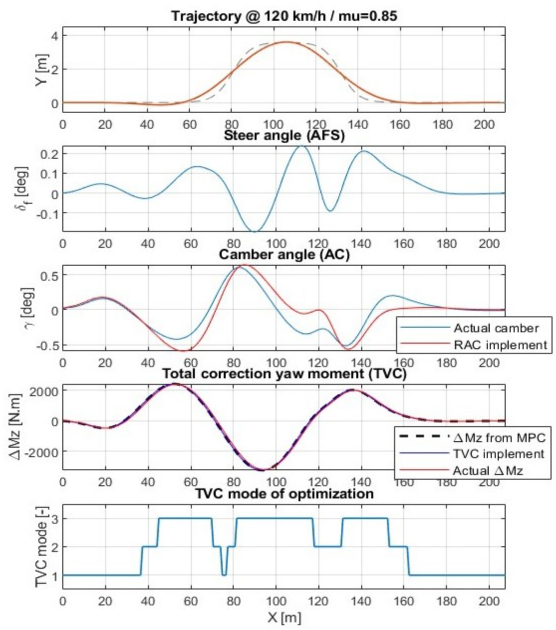


**Figure 8:** Internal dynamics and actuator behavior at 120 km/h




[ DOI: 10.22068/ase.2026.751 ]

The third panel demonstrates the actuation of the rear active camber and highlights the practical complexities of chassis geometry. There is a realistic discrepancy and transient lag between the commanded active camber angle generated by the allocation layer and the actual camber angle executed by the suspension. This discrepancy is intentionally incorporated into the simulation environment by modeling the actuator dynamics as a first-order delay system. In practical hierarchical control frameworks, uncompensated actuator delays and suspension uncertainties can severely degrade vehicle stability, a challenge extensively highlighted in recent advanced robust control studies [35]. However, in our proposed architecture, this actuator lag is inherently compensated by the closed-loop nature of the upper-level MPC. The receding horizon mechanism continuously updates the vehicle states at each sampling instance, dynamically correcting for the tracking errors caused by the lower-level actuator delay.

Finally, the fourth panel validate the efficacy of the torque vectoring system. The Control Allocation (CA) layer successfully translates the virtual corrective yaw moment ($M_z$) demanded by the upper-level MPC into precise longitudinal tire forces ($F_{x,ij}$) via the in-wheel motors. The near-perfect tracking of the desired yaw moment confirms that the system maintains robust path-following and yaw stability, successfully managing the severe non-linearities of vehicle limit handling despite the operational discrepancies and actuator lags.

## 5. Conclusions

In this study, a hierarchical control architecture coordinating Active Front Steering (AFS), Torque Vectoring Control (TVC), and Active Rear Camber (ARC) was developed to enhance path-tracking accuracy and lateral stability under physical limit conditions. Extensive co-simulations in the MATLAB/CarSim environment validated the system's efficacy, yielding specific quantitative improvements.

During a severe 140 km/h Double Lane Change (DLC) maneuver on dry asphalt ($\mu = 0.85$), the fully integrated system (AFS+AC+TVC) minimized the peak lateral tracking error to 0.687 m and the RMS lateral error to 0.239 m, representing improvements of 27% and 32% over the baseline AFS system, respectively. Furthermore, the coordinated approach expanded the maximum achievable lateral acceleration by 18% to 0.8g, while simultaneously reducing the required peak front steering angle by 27% (from 1.85° to 1.34°). Although the peak sideslip angle increased to 7.18° to achieve this trajectory accuracy, the controller successfully regulated the nonlinear dynamics without spin-out. Under low-friction critical conditions ($\mu$ of 0.5 at 60 km/h), the framework preserved stability by significantly bounding the sideslip angle oscillations and reducing the peak steering demand by approximately 1° compared to the standalone AFS.

Analysis of the lower-level Control Allocation (QP) layer confirmed the computational feasibility of the proposed system for real-time implementation. The integrated three-actuator configuration achieved an average execution time of 0.0057 seconds (utilizing 21% of the controller step time) and reduced the peak execution time to 74% of the step limit, successfully avoiding the solver overruns (105% utilization) observed in the conventional AFS+TVC setup. Ultimately, these quantitative findings confirm that the formulated hierarchical control structure efficiently manages severe non-linearities and optimally balances tracking accuracy, dynamic stability, and computational workload. Future work will focus on the experimental validation of this framework on a physical vehicle platform.

## 6. References

[1] Y. Kebbati, N. Ait-Oufroukh, D. Ichalal, and V. Vigneron, "Lateral control for autonomous wheeled vehicles: A technical review," Asian J. Control, vol. 25, no. 4, pp. 2539–2563, 2023.

[2] V. Mazzilli et al., "Integrated chassis control: Classification, analysis and future trends," Annu. Rev. Control, vol. 51, pp. 172–205, 2021.

[3] L. Jin, H. Zhou, X. Xie, B. Guo, and X. Ma, "A direct yaw moment control frame through model predictive control considering vehicle trajectory tracking performance and handling stability for autonomous driving," Control Eng. Pract., vol. 148, p. 105947, 2024.

[4] W. Zhang, Z. Wang, L. Drugge, and M. Nybacka, "Evaluating Model Predictive Path Following and Yaw Stability Controllers for Over-Actuated Autonomous Electric Vehicles," IEEE Trans. Veh. Technol., vol. 69, no. 11, pp. 12807–12821, 2020, doi: 10.1109/TVT.2020.3030863.

[5] P. Stano et al., "Model predictive path tracking control for automated road vehicles: A review," Annu. Rev. Control, vol. 55, pp. 194–236, 2023, doi: https://doi.org/10.1016/j.arcontrol.2022.11.001.





[ DOI: 10.22068/ase.2026.751 ]

[6] W. Tan, M. Wang, and K. Ma, “Research on intelligent vehicle trajectory tracking control based on improved adaptive MPC,” Sensors, vol. 24, no. 7, p. 2316, 2024.

[7] H. Liu, J. Sun, and K. W. E. Cheng, “A two-layer model predictive path-tracking control with curvature adaptive method for high-speed autonomous driving,” IEEE access, vol. 11, pp. 89228–89239, 2023.

[8] Y. Zhang, W. Wang, W. Wang, C. Yang, and Y. Zhang, “An adaptive constrained path following control scheme for autonomous electric vehicles,” IEEE Trans. Veh. Technol., vol. 71, no. 4, pp. 3569–3578, 2022.

[9] Z. Liang, M. Shen, J. Zhao, Z. Li, Y. Wang, and Z. Ding, “Adaptive sliding mode fault tolerant control for autonomous vehicle with unknown actuator parameters and saturated tire force based on the center of percussion,” IEEE Trans. Intell. Transp. Syst., vol. 24, no. 11, pp. 11595–11606, 2023.

[10] P. Hang, X. Xia, G. Chen, and X. Chen, “Active safety control of automated electric vehicles at driving limits: A tube-based MPC approach,” IEEE Trans. Transp. Electrif., vol. 8, no. 1, pp. 1338–1349, 2021.

[11] V. Skrickij, P. Kojis, E. Šabanovič, B. Shyrokau, and V. Ivanov, “Review of integrated chassis control techniques for automated ground vehicles,” Sensors, vol. 24, no. 2, p. 600, 2024.

[12] J. Han, J. Zhang, Z. Yin, M. Iwasaki, Y. Jiang, and H. Wei, “Replanning-Based Nonlinear Model Predictive Tracking Control for Intelligent Vehicle on Unexpected Slippery Road,” IEEE Trans. Ind. Electron., 2025.

[13] N. Guo, X. Zhang, and Y. Zou, “Real-time predictive control of path following to stabilize autonomous electric vehicles under extreme drive conditions,” Automot. Innov., vol. 5, no. 4, pp. 453–470, 2022.

[14] J. Zhao et al., “Constrained fractional-order model predictive control for robust path following of FWID-AGVs with asymptotic prescribed performance,” IEEE Trans. Veh. Technol., vol. 74, no. 2, pp. 2692–2705, 2024.

[15] F. Tarhini, R. Talj, and M. Doumiati, “Holistic adaptive energy-efficient MPC architecture for multi-objective control in over-actuated autonomous vehicles,” Control Eng. Pract., vol. 164, p. 106464, 2025.

[16] E. Hashemi and A. Khajepour, “Integrated path-tracking and combined-slip force controls of autonomous ground vehicles with safe constraints adaptation,” IEEE Trans. Intell. Veh., vol. 9, no. 3, pp. 4265–4274, 2024.

[17] M. Park and S. Yim, “Comparative study on coordinated control of path tracking and vehicle stability for autonomous vehicles on low-friction roads,” in Actuators, MDPI, 2023, p. 398.

[18] G. Wang, L. Liu, Y. Meng, Q. Gu, and G. Bai, “Integrated Path Tracking Control of Steering and Differential Braking Based on Tire Force Distribution,” Int. J. Control. Autom. Syst., vol. 20, no. 2, pp. 536–550, 2022, doi: 10.1007/s12555-021-0117-x.

[19] T. Ahn, Y. Lee, and K. Park, “Design of Integrated Autonomous Driving Control System That Incorporates Chassis Controllers for Improving Path Tracking Performance and Vehicle Stability,” 2021. doi: 10.3390/electronics10020144.

[20] J. Xie, X. Xu, F. Wang, Z. Tang, and L. Chen, “Coordinated control based path following of distributed drive autonomous electric vehicles with yaw-moment control,” Control Eng. Pract., vol. 106, p. 104659, 2021, doi: https://doi.org/10.1016/j.conengprac.2020.104659.

[21] B. Li, C. Lin, J. Ahmadi, E. Siampis, S. Longo, and E. Velenis, “An integrated path-tracking and control allocation method for autonomous racing electric vehicles,” Veh. Syst. Dyn., vol. 62, no. 6, pp. 1517–1540, 2024.

[22] E. Morera-Torres, C. Ocampo-Martinez, and F. D. Bianchi, “Experimental modelling and optimal torque vectoring control for 4WD vehicles,” IEEE Trans. Veh. Technol., vol. 71, no. 5, pp. 4922–4932, 2022.

[23] F. Teng, J. Wang, L. Jin, Z. Wang, Z. Zhou, and Z. Liu, “Cooperative control strategy of trajectory tracking and driving stability for distributed-drive vehicles under extreme conditions,” Control Eng. Pract., vol. 147, p. 105905, 2024.

[24] Y. Li et al., “Trajectory tracking of four-wheel driving and steering autonomous vehicle under extreme obstacle avoidance condition,” Veh. Syst. Dyn., vol. 62, no. 3, pp. 601–622, Mar. 2024, doi: 10.1080/00423114.2023.2186249.

[25] L. Liao, G. Sun, S. Cai, C. Wang, and J. Zheng, “Stable High-Speed Overtaking with Integrated Model Predictive and Four-Wheel Steering Control,” Electronics, vol. 14, no. 6, p. 1133, 2025.



[ DOI: 10.22068/ase.2026.751 ]

[26] S. Yim, “Comparison among active front, front independent, 4-wheel and 4-wheel independent steering systems for vehicle stability control,” Electronics, vol. 9, no. 5, p. 798, 2020.

[27] H. Liu, L. Zhang, P. Wang, and H. Chen, “A real-time NMPC strategy for electric vehicle stability improvement combining torque vectoring with rear-wheel steering,” IEEE Trans. Transp. Electrif., vol. 8, no. 3, pp. 3825–3835, 2022.

[28] P. Hang and X. Chen, “Towards autonomous driving: Review and perspectives on configuration and control of four-wheel independent drive/steering electric vehicles,” in Actuators, MDPI, 2021, p. 184.

[29] W. Zhang, L. Drugge, M. Nybacka, and Z. Wang, “Exploring Active Camber for Path Following and Yaw Stability of Autonomous Vehicles BT - Advances in Dynamics of Vehicles on Roads and Tracks,” M. Klomp, F. Bruzelius, J. Nielsen, and A. Hillemyr, Eds., Cham: Springer International Publishing, 2020, pp. 1491–1499.

[30] W. Zhang, L. Drugge, M. Nybacka, and Z. Wang, “Active camber for enhancing path following and yaw stability of over-actuated autonomous electric vehicles,” Veh. Syst. Dyn., vol. 59, no. 5, pp. 800–821, 2021.

[31] J. Lu, R. Wang, and C. Wan, “Intelligent Vehicle Path Tracking and Stability Control Method Based on Extension Coordinated Control of AFS and DYC,” IEEE Access, vol. 13, pp. 7353–7365, 2025, doi: 10.1109/ACCESS.2025.3527207.

[32] S. Vaskov, R. Quirynen, M. Menner, and K. Berntorp, “Friction-adaptive stochastic nonlinear model predictive control for autonomous vehicles,” Veh. Syst. Dyn., vol. 62, no. 2, pp. 347–371, Feb. 2024, doi: 10.1080/00423114.2023.2219791.

[33] A. D. Damavandi, M. Masih-Tehrani, and B. Mashadi, “Configuration development and optimization of hydraulically interconnected suspension for handling and ride enhancement,” Proc. Inst. Mech. Eng. Part D J. Automob. Eng., vol. 236, no. 2–3, pp. 381–394, 2022.

[34] G. Qi, M. Yue, J. Shangguan, L. Guo, and J. Zhao, “Integrated control method for path tracking and lateral stability of distributed drive electric vehicles with extended Kalman filter–based tire cornering stiffness estimation,” J. Vib. Control, vol. 30, no. 11–12, pp. 2582–2595, 2024.

[35] A. Khosravian, M. Masih-Tehrani, A. Amirkhani, and S. Ebrahimi-Nejad, “Robust autonomous vehicle control by leveraging multi-stage MPC and quantized CNN in HIL Framework,” Appl. Soft Comput., vol. 162, p. 111802, 2024.



[ DOI: 10.22068/ase.2026.751 ]